



The Sloan Digital Sky Survey Reverberation Mapping Project: Photometric g and i Light Curves

K. Kinemuchi¹, Patrick B. Hall², Ian McGreer³, C. S. Kochanek⁴, Catherine J. Grier^{5,6,7}, Jonathan Trump⁸, Yue Shen^{9,10,31}, W. N. Brandt^{6,7,11}, W. M. Wood-Vasey¹², Xiaohui Fan⁵, Bradley M. Peterson^{4,13,14}, Donald P. Schneider^{6,7}, Juan V. Hernández Santisteban¹⁵, Keith Horne¹⁵, Yuguang Chen¹⁶, Sarah Eftekharzadeh¹⁷, Yucheng Guo¹⁸, Siyao Jia¹⁹, Feng Li²⁰, Zefeng Li¹⁸, Jundan Nie²¹, Kara A. Ponder²², Jesse Rogerson^{23,24}, Tianmen Zhang^{21,25}, Hu Zou²¹, Linhua Jiang²⁶, Luis C. Ho^{18,26}, Jean-Paul Kneib^{27,28}, Patrick Petitjean²⁹, Nathalie Palanque-Delabrouille³⁰, and Christophe Yèche³⁰

¹ Apache Point Observatory/New Mexico State University, 2001 Apache Point Road, Sunspot, NM 88349, USA

² Department of Physics and Astronomy, York University, Toronto, Ontario M3J 1P3, Canada

³ Steward Observatory, University of Arizona, 933 North Cherry Avenue, Tucson, AZ 85721-0065, USA

⁴ Department of Astronomy, The Ohio State University, 140 West 18th Avenue, Columbus, OH 43210, USA

⁵ Steward Observatory, The University of Arizona, 933 North Cherry Avenue, Tucson, AZ 85721, USA

⁶ Department of Astronomy and Astrophysics, Eberly College of Science, The Pennsylvania State University, 525 Davey Laboratory, University Park, PA 16802, USA

⁷ Institute for Gravitation & the Cosmos, The Pennsylvania State University, University Park, PA 16802, USA

⁸ Department of Physics, University of Connecticut, 2152 Hillside Road, Unit 3046, Storrs, CT 06269, USA

⁹ Department of Astronomy, University of Illinois at Urbana-Champaign, Urbana, IL 61801, USA

¹⁰ National Center for Supercomputing Applications, University of Illinois at Urbana-Champaign, Urbana, IL 61801, USA

¹¹ Department of Physics, The Pennsylvania State University, University Park, PA 16802, USA

¹² Pittsburgh Particle Physics, Astrophysics, and Cosmology Center (PITT PACC), Physics and Astronomy Department, University of Pittsburgh, Pittsburgh, PA 15260, USA

¹³ Center for Cosmology and AstroParticle Physics, The Ohio State University, 191 West Woodruff Avenue, Columbus, OH 43210, USA

¹⁴ Space Telescope Science Institute, 3700 San Martin Drive, Baltimore, MD 21218, USA

¹⁵ SUPA Physics & Astronomy, University of St. Andrews, Fife, KY16 9SS, Scotland, UK

¹⁶ California Institute of Technology, 1200 East California Boulevard, MC 249-17, Pasadena, CA 91125, USA

¹⁷ Department of Physics and Astronomy, University of Utah, 115 South 1400 East, Salt Lake City, UT 84112, USA

¹⁸ Department of Astronomy, School of Physics, Peking University, Beijing 100871, People's Republic of China

¹⁹ Department of Astronomy, University of California, Berkeley, CA 94720, USA

²⁰ School of Mathematics and Physics, Changzhou University, Changzhou 213164, People's Republic of China

²¹ Key Laboratory of Optical Astronomy, National Astronomical Observatories, Chinese Academy of Sciences, Beijing 100012, People's Republic of China

²² Berkeley Center for Cosmological Physics, University of California Berkeley, 341 Campbell Hall, Berkeley, CA 94720, USA

²³ Canada Aviation and Space Museum, 11 Aviation Parkway, Ottawa, ON, K1K 4Y5, Canada

²⁴ Department of Physics and Astronomy, York University, Toronto, ON M3J 1P3, Canada

²⁵ School of Astronomy and Space Science, University of Chinese Academy of Sciences, People's Republic of China

²⁶ Kavli Institute for Astronomy and Astrophysics, Peking University, Beijing 100871, People's Republic of China

²⁷ Institute of Physics, Laboratory of Astrophysics, Ecole Polytechnique Fédérale de Lausanne (EPFL), Observatoire de Sauverny, 1290 Versoix, Switzerland

²⁸ Aix Marseille Université, CNRS, LAM (Laboratoire d'Astrophysique de Marseille) UMR 7326, F-13388, Marseille, France

²⁹ Institut d'Astrophysique de Paris, Sorbonne Université et CNRS, 98bis Boulevard Arago, F-75014, Paris, France

³⁰ IRFU, CEA, Université Paris-Saclay, F-91191 Gif-sur-Yvette, France

Received 2020 May 22; revised 2020 July 1; accepted 2020 July 6; published 2020 September 3

Abstract

The Sloan Digital Sky Survey (SDSS) Reverberation Mapping program monitors 849 active galactic nuclei (AGNs) both spectroscopically and photometrically. The photometric observations used in this work span over 4 yr and provide an excellent baseline for variability studies of these objects. We present the photometric light curves from 2014 to 2017 obtained by the Steward Observatory's Bok telescope and the Canada–France–Hawaii telescope with MegaCam. We provide details on the data acquisition and processing of the data from each telescope, the difference imaging photometry used to produce the light curves, and the calculation of a variability index to quantify each AGN's variability. We find that the Welch–Stetson J index provides a useful characterization of AGN variability and can be used to select AGNs for further study.

Unified Astronomy Thesaurus concepts: Active galactic nuclei (16)

Supporting material: machine-readable table, tar.gz file

1. Introduction

The variability of active galactic nuclei (AGNs; hereafter synonymously used with “quasar”) is one of the most powerful tools available to explore the physical processes in these objects and to determine their role in the evolution of galaxies (e.g., Ulrich et al. 1997; Vanden Berk et al. 2004; MacLeod et al. 2010).

Various aspects of quasar variability touch on a wide range of physical processes (Kozłowski et al. 2010), and studies span a wide breadth of topics, ranging from continuum variability and the exploration of quasar accretion processes (e.g., Clavel et al. 1991; Krolik et al. 1991; Czerny et al. 1999; Kelly et al. 2011), to emission-line variability and the broad-line region (e.g., Blandford & McKee 1982; Peterson 1993; Kaspi et al. 2000; Sun et al. 2015), to the study of so-called “changing-look” AGNs (e.g., Tohline & Osterbrock 1976; Cohen et al. 1986; Clavel et al. 1989;

³¹ Alfred P. Sloan Research Fellow.

Denney et al. 2014; Shappee et al. 2014; LaMassa et al. 2015; MacLeod et al. 2016), and to studies of absorption-line variability (e.g., Smith & Penston 1988; Turnshek et al. 1988; Barlow 1993; Lundgren et al. 2007; Filiz et al. 2013). AGN variability/monitoring programs provide important insights into the nature of the inner regions of quasars on a variety of scales, leading to better understanding of their role in the evolution of AGNs and galaxies. There are many time-series data sets that focus on AGNs over a variety of scales. Most spectroscopic monitoring projects, by necessity, have focused either on small numbers of AGNs at high cadence or large numbers of AGNs at very low cadence. While there are science goals that can be accomplished by both types of data sets, statistical interpretations are limited by the small sample sizes in the first case, and detailed investigations are limited by the small numbers of epochs in the second case. Recently, however, large surveys that use multi-object spectrographs have begun to target statistically significant samples of representative quasar populations for much higher cadence, long-duration studies (e.g., King et al. 2015).

The Sloan Digital Sky Survey Reverberation Mapping (SDSS-RM) project (Shen et al. 2015a) is an ongoing program that monitors 849 broad-line quasars/AGNs. The project is based on a spectroscopic campaign using the Baryon Oscillation Spectroscopic Survey (BOSS) spectrographs (Smee et al. 2013) that began at the end of the SDSS-III survey and continues through the SDSS-IV survey (Blanton et al. 2017). As of summer 2019, the program has accumulated 6 yr of SDSS spectroscopic data. To complement the spectroscopic data, the SDSS-RM field has been photometrically monitored at the Canada–France–Hawaii (CFHT) and Steward Observatory Bok telescopes. The SDSS-RM field was observed in the SDSS *g* and *i* bandpasses with the CFHT from 2014 to 2016 and with the Bok from 2014 through 2017. In addition, the field was monitored photometrically as a part of the Panoramic Survey Telescope and Rapid Response System (Pan-STARRS1) Medium Deep field 7 (MD07) program during 2010–2013, which extends the total time baseline to 9 yr. This program will continue to be observed through 2020, and monitoring of this field will continue as a part of the SDSS-V black hole Mapper project (BHM; Kollmeier et al. 2017).

RM (Blandford & McKee 1982; Peterson et al. 2004) is the primary objective of the SDSS-RM program. RM uses the time delays between the variability of emission from different regions within the AGN. For example, optical continuum variations are echoed by emission lines from the broad-line region (BLR), but with a time delay corresponding to the time it takes for light to travel to the BLR from the continuum-emitting region. This information yields a characteristic radius of the BLR gas, which can be combined with an orbital velocity estimate from the width of the broad emission lines to estimate the black hole mass.

The main goals of SDSS-RM are to obtain reverberation mapping BLR time-lag measurements and to estimate black hole masses for hundreds of quasars. Technically, these goals require only spectroscopic monitoring. However, the cadence of the SDSS-RM spectroscopy, while higher than any previous study of such a large sample, is by itself inadequate. Supplemental photometric monitoring of the SDSS-RM field is critical, as the additional photometry can better sample the continuum light curves, led by improved sensitivity to shorter time lags and improved accuracy for longer lags. In addition, the photometry can be used to improve the spectrophotometric

calibration of the spectroscopy. Simulations and real data analyses thus far indicate that the additional photometry will allow us to nearly double the number of lag determinations compared to only using the spectroscopic data (Shen et al. 2015a, 2016a; Grier et al. 2017).

The SDSS-RM program has reported ~ 100 additional broad-line lag measurements (Shen et al. 2016b; Grier et al. 2017, 2019). In addition, the SDSS-RM collaboration has produced a wide variety of results using the first 1–4 yr of data, including studies of broad absorption-line variability, host-galaxy properties, emission-line velocity shifts, and quasar variability (Grier et al. 2015, 2017; Matsuoka et al. 2015; Shen et al. 2015b, 2016a, 2016b; Sun et al. 2015, 2018; Denney et al. 2016a, 2016b; Li et al. 2017; Yue et al. 2018; Hemler et al. 2019; Wang et al. 2019). However, there will be many other scientific applications for a data set containing more than 70 spectroscopic epochs over a period of several years with more than 100 epochs of accompanying photometric observations of a sample of 849 quasars that span a wide range in redshift ($0.1 < z < 4.5$) and were chosen to span a wide range of quasar properties (see Shen et al. 2019).

In this work, we present the details of the photometric data from the CFHT and Bok telescopes obtained during the first 4 yr of the SDSS-RM program. Details of the telescopes and the strategy for data collection at both facilities are described in Section 2. The data sets were individually preprocessed by their respective facilities’ pipelines (see the subsections in Section 2). The light curves were produced using the ISIS difference imaging packages (Alard 2000) described in Section 3. We present in Section 4 the light curves for all 849 SDSS-RM targets and an additional 365 AGNs that were also monitored as a part of the program by the Bok telescope. In Section 5 we calculate a variability index to quantify the variability of each object and to identify which objects have a highly variable continuum. We conclude this paper in Section 6 with a summary of our work and provide a synopsis of future studies.

2. Data Collection

2.1. CFHT Observations

The CFHT/MegaCam (Aune et al. 2003) is a wide-field optical imager with a pixel scale of $0''.187$. Its field of view (FoV) was expanded from 1 deg^2 (36 charge-coupled devices (CCDs)) to 1.1 deg^2 (40 CCDs) in 2015. All MegaCam observations were made in the Queued Service Observations (QSO) mode, and a log of the observations is presented in Table 1. Each semester’s observations at the CFHT are discussed in the appropriate section below. Raw and calibrated CFHT/MegaCam images can be retrieved from the Canadian Astronomy Data Centre using the proposal IDs given below.³²

2.1.1. CFHT Pointings Layout

The SDSS-RM field overlaps with the W3 wide-field and the D3 deep-field of the CFHT Legacy Survey (Semboloni et al. 2006).³³ To cover the footprint of the 7° SDSS-RM field, we used a total of nine slightly overlapping pointings

³² <http://www.cadc-ccda.hia-ihp.nrc-cnrc.gc.ca/en/cfht/>

³³ See <http://www.cfht.hawaii.edu/Science/CFHTLS/T0007/T0007-docs10.html>.

Table 1
Log of CFHT Observations

MJD (days)	UT Date	Filter	Avg Seeing (arcsec)	Weather	Comment
2014A					
56712	20140224	<i>g, i</i>	0.7	Photometric	Partial coverage
56715	20140227	<i>g, i</i>	1.0	Photometric	
56721	20140305	<i>g</i>	1.2	Photometric	
56722	20140306	<i>g, i</i>	0.7	Photometric	
56723	20140307	<i>g, i</i>	0.6	Thin cirrus	
56741	20140325	<i>g, i</i>	1.0	Thin cirrus	Partial coverage
56743	20140327	<i>g</i>	0.8	Photometric	
56744	20140328	<i>g, i</i>	0.7	Photometric	
56751	20140404	<i>g, i</i>	0.7	Photometric	
56772	20140425	<i>g</i>	0.9	Thin cirrus	
56776	20140429	<i>g, i</i>	0.6	Photometric	Partial coverage in <i>i</i>
56778	20140501	<i>g, i</i>	0.7	Photometric	
56780	20140503	<i>g, i</i>	0.4	Thin cirrus	
56781	20140504	<i>g, i</i>	0.5	Thin cirrus	
56783	20140506	<i>g, i</i>	0.5	Partly cloudy	
56798	20140521	<i>g, i</i>	0.6	Photometric	Partial coverage in <i>i</i>
56801	20140524	<i>g, i</i>	0.8	Photometric	
56803	20140526	<i>g</i>	0.9	Thin cirrus	
56805	20140528	<i>g, i</i>	0.7	Photometric	
56807	20140530	<i>g, i</i>	0.8	Photometric	
56809	20140601	<i>g</i>	0.8	Photometric	Partial coverage (CFHTLS D3)
56811	20140603	<i>g, i</i>	0.5	Photometric	
56829	20140621	<i>g, i</i>	0.6	Photometric	
56831	20140623	<i>g, i</i>	0.5	Photometric	
56833	20140625	<i>g, i</i>	0.6	Photometric	
56835	20140627	<i>g, i</i>	0.6	Photometric	Partial coverage in <i>i</i>
56837	20140629	<i>g, i</i>	0.6	Photometric	
56839	20140701	<i>g, i</i>	0.8	Photometric	
56841	20140703	<i>g, i</i>	0.6	Thin cirrus	
56865	20140727	<i>g, i</i>	0.8	Photometric	
2015A					
57078	20150225	<i>g</i>	1.0	Photometric	Short exposures only
57104	20150323	<i>g</i>	0.6	Partly cloudy	
57105	20150324	<i>g</i>	0.8	Photometric	
57123	20150411	<i>g</i>	0.8	Thin cirrus	
57133	20150421	<i>g</i>	0.8	Photometric	
57134	20150422	<i>g</i>	1.0	Thin cirrus	Partial coverage
57157	20150515	<i>g, i</i>	1.0	Photometric	
57160	20150518	<i>g, i</i>	0.8	Thin cirrus	
57166	20150524	<i>g</i>	0.7	Photometric	
57185	20150612	<i>g</i>	1.0	Photometric	
57191	20150618	<i>g</i>	1.0	Photometric	Partial coverage in <i>i</i>
57213	20150710	<i>g, i</i>	1.0	Photometric	
57216	20150713	<i>g, i</i>	1.0	Photometric	
57217	20150714	<i>i</i>	0.9	Photometric	
57220	20150717	<i>g, i</i>	1.0	Thin cirrus	
57221	20150718	<i>i</i>	0.5	Photometric	Partial coverage in <i>i</i>
57223	20150720	<i>g, i</i>	0.8	Photometric	
2016A					
57420	20160202	<i>g, i</i>	0.9	Photometric	
57433	20160215	<i>g, i</i>	0.6	Photometric	
57479	20160401	<i>g, i</i>	0.6	Photometric	
57492	20160414	<i>g, i</i>	1.1	Photometric	
57508	20160430	<i>g, i</i>	0.9	Photometric	

Table 1
(Continued)

MJD (days)	UT Date	Filter	Avg Seeing (arcsec)	Weather	Comment
57520	20160512	<i>g, i</i>	0.6	Thin cirrus	
57542	20160603	<i>g</i>	0.8	Photometric	
57543	20160604	<i>i</i>	0.6	Photometric	
57547	20160608	<i>g</i>	0.6	Photometric	
57567	20160628	<i>g</i>	0.9	Partly cloudy	
57568	20160629	<i>i</i>	0.9	Thin cirrus	Partial coverage
2017A					
57806	20170222	<i>g</i>	1.0	Photometric	Partial coverage
57807	20170223	<i>g</i>	1.0	Photometric	
57833	20170321	<i>g</i>	0.9	Photometric	
57840	20170328	<i>g</i>	0.8	Photometric	
57843	20170331	<i>g</i>	0.7	Photometric	
57846	20170403	<i>g</i>	0.8	Photometric	
57862	20170419	<i>g</i>	0.8	Photometric	
57868	20170425	<i>g</i>	0.9	Partly cloudy	
57871	20170428	<i>g</i>	0.7	Photometric	
57875	20170502	<i>g</i>	1.1	Thin cirrus	
57877	20170504	<i>g</i>	0.8	Photometric	
57890	20170517	<i>g</i>	0.7	Photometric	
57894	20170521	<i>g</i>	0.6	Thin cirrus	
57903	20170530	<i>g</i>	0.6	Thin cirrus	
57924	20170620	<i>g</i>	1.0	Photometric	
57950	20170716	<i>g</i>	0.8	Thin cirrus	
57964	20170730	<i>g</i>	0.8	Photometric	

Note. “Partial coverage” indicates not all RM pointings were imaged that epoch. Epochs MJD = 56829 and 56865 were pointings to observe additional calibration sources in the CFHTLS D3 field, which partially covers the RM field. The Weather column refers to the weather status during our observations that night and is taken from the searchable CFHT QSO Night Reports and Program Status available at <http://www.cfht.hawaii.edu/en/science/QSO/#nr>; where more than one weather condition is noted during our observations, we cite the worst condition reported.

labeled A through I with two dither positions at each pointing to fill in the CCD gaps. The sky coordinates of the centers of the 18 different dither positions (labeled A1 through I2) are given in Table 2. The layout of the fields is shown in Figure 1(a) for 2014A–2015A (36 unvignetted CCDs) and in Figure 1(b) for 2016A–2017A (40 unvignetted CCDs). Two exposures were taken at each dither position. The first was a fixed 30 (40) s short exposure in *g* (*i*) for bright RM targets. The second had an exposure time determined dynamically to achieve a desired point-source signal-to-noise ratio (S/N) of 25 at $i = 22$ and $g = 22.25$, given the seeing and transparency at the time of the observation. At CFHT, this procedure is known as the “Queued Service Observations–Signal-to-Noise” mode. The average dynamic exposure lengths in 2014A were 55 s in *g* and 77 s in *i*.

2.1.2. Observing Semester 2014A (Proposal 14AC02)

A total of 81.4 hr was awarded from Canada, France, and China, and 52.2 hr of data were obtained. The observations were made using the CFHT filters *g*.MP9401 and *i*.MP9702.³⁴

³⁴ See <http://www.cfht.hawaii.edu/Instruments/Filters/megaprime.html>.

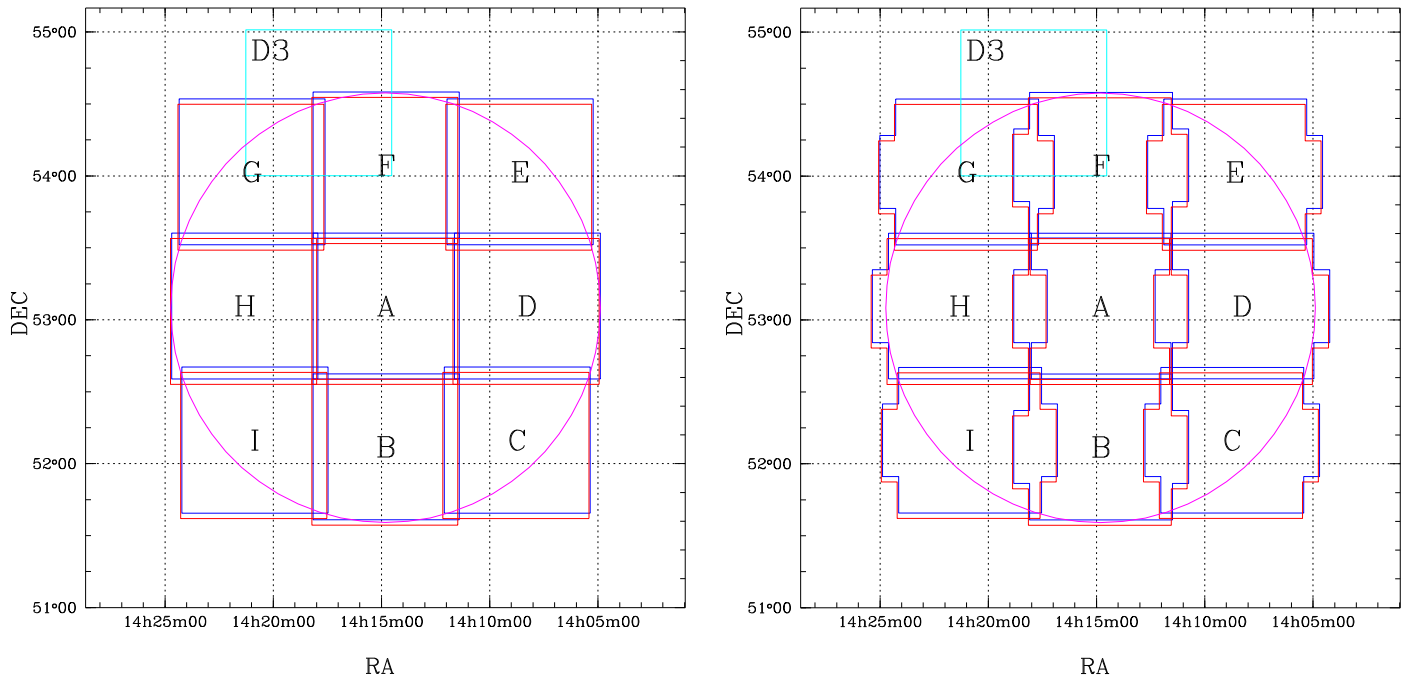


Figure 1. RM field pointing layout. The magenta circle is the SDSS–BOSS spectrograph FoV. The SDSS–RM field is contained within the CFHTLS W3 (wide) field and partially overlaps the CFHTLS D3 (deep) field, indicated by the cyan square labeled “D3.” The letters denote the positions of each of the nine pointings and the order in which they are observed. The blue and red outlines are the two dithered exposures at each pointing. Each pointing overlaps the next by $\geq 16''/5$ in R.A. and $\geq 88''/5$ in decl. The left panel shows the imaged areas of the FoV for semesters 2014A and 2015A, when 36 CCDs were unvignetted. The right panel shows imaged areas of the FoV for semesters 2016A and 2017A, when 40 CCDs were unvignetted. Both are approximate, in that they do not account for the small change in the extent R.A. of the MegaCam FoV over the range in decl. shown.

Table 2
CFHT Pointing Centers

Position	R.A.	Decl.
A1	14:14:47.17	+53:05:46.0
A2	14:14:50.83	+53:03:31.0
B1	14:14:47.19	+52:07:00.5
B2	14:14:50.81	+52:04:45.5
C1	14:08:43.77	+52:09:50.0
C2	14:08:47.54	+52:07:35.0
D1	14:08:15.56	+53:05:46.0
D2	14:08:19.40	+53:03:31.0
E1	14:08:35.77	+54:01:42.0
E2	14:08:39.63	+53:59:27.0
F1	14:14:47.15	+54:04:31.5
F2	14:14:50.85	+54:02:16.5
G1	14:20:58.53	+54:01:42.0
G2	14:21:02.07	+53:59:27.0
H1	14:21:18.77	+53:05:46.0
H2	14:21:22.26	+53:03:31.0
I1	14:20:50.61	+52:09:50.0
I2	14:20:54.08	+52:07:35.0

In each MegaCam run, the g and i observations were executed in Observation Groups (OGs). Completion of the g observation group triggered, via a relational execution link (REEL), an i observation group to be executed within 12 hr (24 hr in December/January and June/July). On most occasions, the g and i OGs were executed on the same night. If no i epoch was obtained within 24 hr of a g epoch, the i epoch was skipped in favor of a new g epoch two nights later. Under poor weather conditions, the requested cadence increased to nightly near the end of a MegaCam run to try to obtain a minimum of 4 epochs.

2.1.3. Observing Semester 2015A (Proposal 15AS02)

A total of 20.4 hr was awarded from Canada, France, and China, and 15.5 hr of data were obtained. At the beginning of 2015A, Megacam was upgraded from 36 to 40 CCDs. New filters that allowed unvignetted observations of the entire FoV were also installed. For our observations, however, we wished to avoid any changes in photometry due to bandpass differences; thus, we continued to use the same filters as in 2014A. In this semester, we tried to obtain two g -band epochs per MegaCam run, separated by 4–10 days. Additional g -band epochs could be added to a run if the time allocated for our observations in previous MegaCam runs had gone unused. An i -band epoch was requested to occur either within 15 hr after a g -band epoch or not at all.

2.1.4. Observing Semester 2016A (Proposal 16AC12)

A total of 20.4 hr was awarded from Canada, France, and China, and 15.8 hr of data were obtained. Beginning with semester 2016A, we used the new filters (CFHT filters g , MP9402 and i , MP9703³⁵) for an unvignetted view of the upgraded focal plane with 40 CCDs. However, we have not yet processed the photometric measurements of the target quasars using images from the four new CCDs. We used the same scheduling pattern as in semester 2015A.

2.1.5. Observing Semester 2017A (Proposals 17AC12 + 17AF13)

A total of 16 hr was awarded from Canada and France, and 12 hr of data were obtained. Due to a smaller time allocation in

³⁵ See <http://www.cfht.hawaii.edu/Instruments/Filters/megaprime.html>.

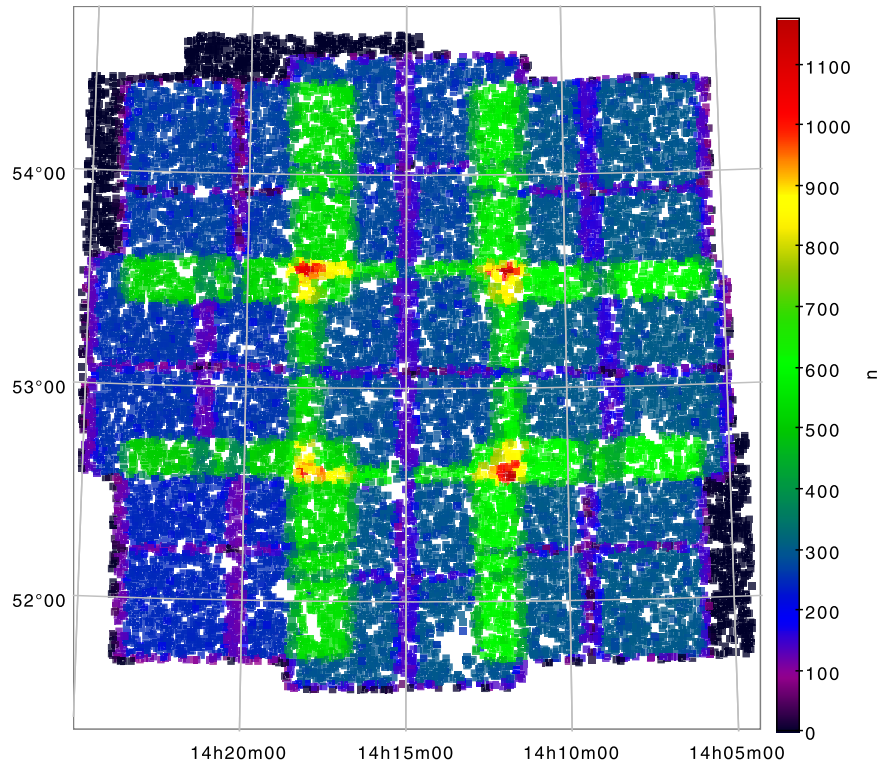


Figure 2. Number of observations of individual standard stars in the Bok observations of the SDSS-RM field, including data obtained during 2014–2016. The patterns due to the pointing sequence are clearly visible: dark blue regions are observed only once during a pointing sequence, and light blue regions are observed twice due to the overlap in dithered frames at each of the nine primary pointing centers. Green regions are overlaps between the nine pointing centers, resulting in twice as many observations per star. Finally, the yellow/red regions near the center are where four or more pointings overlap. Holes are regions around bright stars. Over the 3 yr period, individual stars received anywhere from ~ 200 to $\gtrsim 1000$ photometric measurements.

2017A, we chose to request only *g*-band observations. After the entire field was observed, at least 72 hr were required to elapse before it could be observed again. Results incorporating these data will be presented at a future date.

2.2. Bok Observations

Monitoring of the SDSS-RM field with Steward Observatory’s 2.3 m Bok telescope commenced in 2013 December and is ongoing. The SDSS-RM observations were allocated time through the regular proposal process and observing nights were often shared with other programs to maximize time coverage and observing efficiency. SDSS-RM data are collected with the 90Prime instrument (Williams et al. 2004), a $\sim 1^\circ$ FoV. As with the CFHT observations, Bok data are collected in the SDSS *g* and *i* bandpasses. To complement the CFHT dark time observations and provide the continuous photometric coverage, the Bok observations were typically obtained during bright lunar phases, including full Moon. The sky background is thus quite high, which degrades the overall sensitivity. Each Bok pointing has a design exposure time of 300 s, but this time was sometimes divided into multiple exposures to keep the bright sky background well below saturation limits.

The 90Prime FoV covers the SDSS-RM field in nine total pointings. To better cover CCD gaps and to compensate the high backgrounds, these pointings are divided into two exposures (typically 150 s, as above) that are dithered by a few arcminutes, leading to a total of 18 pointings per epoch. Usually only one bandpass is used per night and filter changes occur on adjacent nights. An exception is the three nights

around full Moon, where only the *i* band is used due to the high background at shorter wavelengths. Collecting all 18 pointings takes roughly two hours with overhead for focus and pointing alignment. The pointing sequence is repeated through the night as time permits. Given the overlap between pointings as well as the repeated passes, an individual quasar receives anywhere from 1 to ~ 10 observations in a single night, allowing for analyses of short-timescale variability. The observation pattern is presented in Figure 2, demonstrating that regions within the SDSS-RM field received between ~ 200 and $\gtrsim 1000$ observations over the 3 yr period beginning with the 2014 campaign, obtained from over 5000 individual exposures. Table 3 provides the log of the Bok observations over the 4 yr.

2.2.1. Bok Data Reductions

Bok 90Prime data were processed using standard optical image processing techniques implemented in a Python-based pipeline developed by our group.³⁶ The pipeline organizes data by observing night and automatically identifies the calibration frames taken for each night. Bias and dome flat correction frames are produced by a stacked median of ~ 10 calibration frames. The science frames are sorted by filter and associated with the calibration frames that are nearest in time. The overscan region of each science image is collapsed to 1D using a median, followed by a 17 pixel wide median filter to smooth the overscan pattern. The resulting vector is subtracted from the

³⁶ <https://github.com/imcgreer/idrm> and <https://github.com/legacysurvey/rapala>.

Table 3
Log of Bok Observations

MJD (days)	UT Date	Filter(s)	Ave. Seeing (arcsec)	Comment
2014A				
56648	20131222	<i>g</i>	3.0	Partial coverage
56671	20140114	<i>g</i>	1.5	
56672	20140115	<i>i</i>	1.7	
56673	20140116	<i>i</i>	1.7	
56674	20140117	<i>i</i>	1.4	
56675	20140118	<i>g</i>	1.4	
56677	20140120	<i>g</i>	1.5	Partial coverage, partly cloudy
56678	20140121	<i>g, i</i>	1.2	
56680	20140123	<i>g, i</i>	1.7	Thin clouds
56683	20140126	<i>g, i</i>	1.4	
56685	20140128	<i>g</i>	1.5	
56686	20140129	<i>i</i>	1.3	Cloudy
56701	20140213	<i>g</i>	1.7	Thin clouds
56702	20140214	<i>i</i>	1.5	Thin clouds
56703	20140215	<i>i</i>	1.4	
56705	20140217	<i>g</i>	1.4	Partial coverage, cloudy
56706	20140218	<i>g</i>	1.6	
56707	20140219	<i>i</i>	1.8	Partly cloudy
56728	20140312	<i>g</i>	1.5	
56729	20140313	<i>i</i>	1.2	Thin clouds
56730	20140314	<i>g</i>	2.0	Cloudy
56731	20140315	<i>i</i>	1.3	
56732	20140316	<i>i</i>	2.5	Windy
56733	20140317	<i>i</i>	1.4	
56734	20140318	<i>g</i>	1.5	
56760	20140413	<i>g</i>	2.2	Partly cloudy with wind
56761	20140414	<i>i</i>	1.4	Partly cloudy with wind
56762	20140415	<i>g, i</i>	1.8	
56763	20140416	<i>i</i>	1.0	
56764	20140417	<i>g</i>	1.9	
56771	20140424	<i>g</i>	1.6	Partly cloudy
56772	20140425	<i>i</i>	1.2	
56773	20140426	<i>g</i>	1.9	Partial coverage, cloudy
56774	20140427	<i>g</i>	1.7	
56775	20140428	<i>i</i>	1.5	
56789	20140512	<i>g</i>	2.2	
56790	20140513	<i>g</i>	2.1	
56791	20140514	<i>i</i>	2.0	
56792	20140515	<i>i</i>	1.3	
56793	20140516	<i>g</i>	1.6	Thin clouds
56794	20140517	<i>g</i>	1.3	Thin clouds
56795	20140518	<i>g, i</i>	1.4	Thin clouds with wind
56817	20140609	<i>g</i>	1.4	
56818	20140610	<i>g</i>	1.4	
56819	20140611	<i>g, i</i>	1.9	
56820	20140612	<i>i</i>	1.1	Partly cloudy
56821	20140613	<i>i</i>	1.7	
56838	20140630	<i>g</i>	1.5	
56839	20140701	<i>i</i>	1.3	
56840	20140702	<i>g</i>	1.5	
56855	20140717	<i>i</i>	1.3	Partly cloudy
56856	20140718	<i>g</i>	1.9	
2015A				
57031	20150109	<i>g</i>	1.7	Partly cloudy
57032	20150110	<i>g</i>	2.1	
57057	20150204	<i>g</i>	1.5	
57058	20150205	<i>i</i>	1.5	
57062	20150209	<i>g</i>	1.5	

Table 3
(Continued)

MJD (days)	UT Date	Filter(s)	Ave. Seeing (arcsec)	Comment
57063	20150210	<i>i</i>	1.3	
57087	20150306	<i>g</i>	2.5	
57088	20150307	<i>i</i>	1.7	
57116	20150404	<i>g, i</i>	1.5	Partial coverage in <i>g</i> , cloudy
57117	20150405	<i>g, i</i>	1.8	Partly cloudy
57148	20150506	<i>i</i>	1.6	Partly cloudy
57149	20150507	<i>g</i>	2.2	Partial coverage, cloudy
57150	20150508	<i>i</i>	2.1	
57170	20150528	<i>g, i</i>	1.5	
57171	20150529	<i>g, i</i>	1.9	Partial coverage in <i>g</i>
57211	20150708	<i>g, i</i>	1.9	Partial coverage in <i>i</i>
57212	20150709	<i>i</i>	1.4	Partial coverage
2016A				
57417	20160130	<i>g, i</i>	1.6	Partly cloudy
57435	20160217	<i>g</i>	3.0	
57451	20160304	<i>g</i>	1.1	Partial coverage, cloudy
57467	20160320	<i>g, i</i>	1.3	Cloudy
57480	20160402	<i>g</i>	1.7	Partial coverage
57481	20160403	<i>g</i>	1.7	Partial coverage, cloudy
57494	20160416	<i>g</i>	3.1	Partial coverage
57509	20160501	<i>g</i>	2.0	Partial coverage
57522	20160514	<i>g</i>	1.8	Partly cloudy
57523	20160515	<i>i</i>	2.6	Cloudy
57535	20160527	<i>g</i>	1.4	
57551	20160612	<i>g</i>	1.4	
57578	20160709	<i>g, i</i>	2.3	Partial coverage in <i>g</i>
57579	20160710	<i>g</i>	2.2	Partial coverage, cloudy
2017A				
57788	20170204	<i>g</i>	1.5	Partial coverage, cloudy
57798	20170214	<i>i</i>	1.6	Partial coverage
57806	20170222	<i>g</i>	1.4	Partial coverage
57818	20170306	<i>g</i>	2.1	Cloudy
57830	20170318	<i>i</i>	1.2	Partial coverage
57831	20170319	<i>g, i</i>	1.2	Partial coverage in <i>i</i> , partly cloudy
57847	20170404	<i>g</i>	2.3	
57848	20170405	<i>i</i>	1.4	
57855	20170412	<i>g, i</i>	1.5	
57895	20170522	<i>g</i>	1.8	
57904	20170531	<i>g</i>	1.3	Partial coverage, cloudy
57905	20170601	<i>g</i>	2.1	Cloudy
57907	20170603	<i>g</i>	1.6	
57920	20170616	<i>g</i>	1.7	
57921	20170617	<i>i</i>	1.5	
57960	20170726	<i>g</i>	1.9	Partly cloudy

image. The 2D bias frame is then subtracted, and the dome flat is applied to the images.

The four 90Prime CCDs each have four readout channels with independent amplifiers. The next step is to combine the 16 image channels into a single, four CCD mosaic with the necessary gain corrections. We found that there are small gain variations over the course of a night and that tracking these variations is necessary to obtain a uniform sky background. To remove sensitivity to illumination gradients, we selected small windows of pixels along the borders of adjacent images and

then fit for the multiplicative factor needed to balance the sky levels of the associated amplifiers. Once the four amplifiers in each CCD were balanced to a common level, we used a similar procedure to fit the sky levels near the center of the field in order to match the CCD sky levels.

The dome screen illumination pattern is quite different than the night sky illumination, so the science images from each night are combined into a filter specific illumination correction. This correction is obtained by scaling each image to a common sky background level and stacking with a clipped mean. The image is binned by a factor of 8 along each axis using a median to remove small objects (stars and galaxies). A smooth 2D spline is then iteratively fit to this rebinned image, removing outlier pixels. The final result is applied to the science images and results in a highly uniform sky background.

For the *i*-band images, we also create a fringe pattern image. The median sky level is removed from each image, and the images are stacked to produce the fringe master. The sky-subtracted images are divided by the fringe master to determine the scaling of the pattern that matches the fringe amplitudes in each frame. Then, the scaled fringe master image is subtracted from the original science frame (prior to removing the median sky level).

A final, high S/N sky flat is constructed from the science frames by median combining the images scaled by the sky background after masking bright objects identified using Source Extractor (Bertin & Arnouts 1996). This sky flat is usually composed of images from a single observing run, unless there are too few ($\lesssim 100$), in which case they are combined over multiple runs. Although the corrections in the sky flats are small (few percent), there are notable patterns remaining after the previous processing steps that the sky flat is able to correct.

The final detrending step is to remove a low-level variable gradient in the sky by fitting a linear 2D spline to the sky background of each image after masking objects. Only the gradient is subtracted; the mean sky level of each image is preserved. Object catalogs are generated using SExtractor and then Scamp (Bertin 2006) is used for astrometric registration. A catalog of astrometric references for the field was initially constructed from SDSS and later updated to use Gaia data release 1 (DR1) positions (Lindgren et al. 2016). The resulting rms in star positions is $\sim 0''.05$.

The pipeline utilizes multiprocessing to run processing steps in parallel. On a typical multicore desktop machine, the entire set of >5000 images can be processed in roughly one day.

2.2.2. Photometric Analysis

Although the primary source of photometry for SDSS-RM is the difference imaging catalogs, we also performed aperture photometry on the Bok images. Locations of both reference stars from SDSS and the RM quasar targets were identified using the world coordinate system (WCS) solutions from the processing pipeline. A set of apertures from $0''.9$ to $10''.1$ were placed at each target location and counts within the apertures were obtained with *sep*.³⁷ We primarily focus on the $2''.3$ and $6''.8$ apertures, which provide roughly optimal and total light apertures for typical Bok seeing.

We construct light curves for all targets. The reference stars are treated as constant sources and are a valuable cross-check on processing errors or poor quality imaging that leads to photometric outliers. For each reference star, we determine a

median magnitude and rms scatter, and then flag measurements that are $> 5\sigma$ outliers. If a single image contains a large number of outliers, we examine it by eye. Most of these cases are images affected by strong scattered light from the bright Moon during the Bok observations, and they are removed from our analysis. Once the data set is cleaned of bad epochs, we determine photometric zero-points and color terms relative to the SDSS *g* and *i*-band photometry of the field using bright ($g < 17$ and $i < 19$ mag) stars.

After removing outliers, we find that the internal accuracy of the Bok photometry reaches ~ 10 mmag for bright stars (17 mag), and ~ 30 mmag at $g = 19$. This suggests we have met our goal for photometric accuracy and that the Bok photometry will be suitable for tracking quasar variability.

3. Difference Imaging

For the analysis of the data sets collected at the CFHT and Bok telescopes, we used the ISIS difference imaging package (Alard & Lupton 1999; Alard 2000).³⁸ To produce the differential flux light curves, the reduced data were parsed into separate FITS files, separated by field, CCD, and bandpass. The CFHT data had nine fields while the Bok data had 18. The CFHT and Bok data sets were processed with ISIS separately.

The images for each subfield are first interpolated to a common frame. Next, a reference image is constructed using the images with the best seeing, lower sky backgrounds, and high transparencies. For each individual image, the reference image is convolved to match its point-spread function (PSF) structure, and the individual image is scaled and subtracted from that convolved reference image to create a difference image on the flux scale of the reference image. Negative values in a difference image indicates that a source is brighter than on the reference image. Details of the convolution matrix and their applications are described in Alard & Lupton (1998) and Alard (2000).

The RM targets and a selection of standard stars were identified on the reference image, and PSF photometry was performed at those positions. Using the midpoint of the image observation (in terms of Modified Julian Date (MJD)) as our time index, light curves were constructed with the differential flux values from ISIS. In this paper, we present the differential flux light curves for each SDSS-RM quasar from each field in which it appears on that field's reference image. Grier et al. (2017) describe how for their analysis, they merged these differential light curves from the different data sets and corrected the uncertainties reported by ISIS using the standard star observations.

3.1. CFHT Processing

For the CFHT data spanning 2014 to 2016, the raw data were detrended with the Elixir pipeline. With the detrended data, we separated the multi-extension FITS files into the individual CCD images (36 for the 2014 data set and 40 for the subsequent years). Processing was systematically performed per field, per pointing (1 or 2), per filter (*g* or *i* band), and per CCD. Source Extractor (Bertin & Arnouts 1996) was used to identify the best subset of the images to create the reference image, based on the sky background and the median FWHM. The number of images selected to construct the reference image ranged between 4 and 10. For some subfields, a bright

³⁷ <https://github.com/kbarbary/sep>

³⁸ The software can be downloaded from <http://www2.iap.fr/users/alard/package.html>.

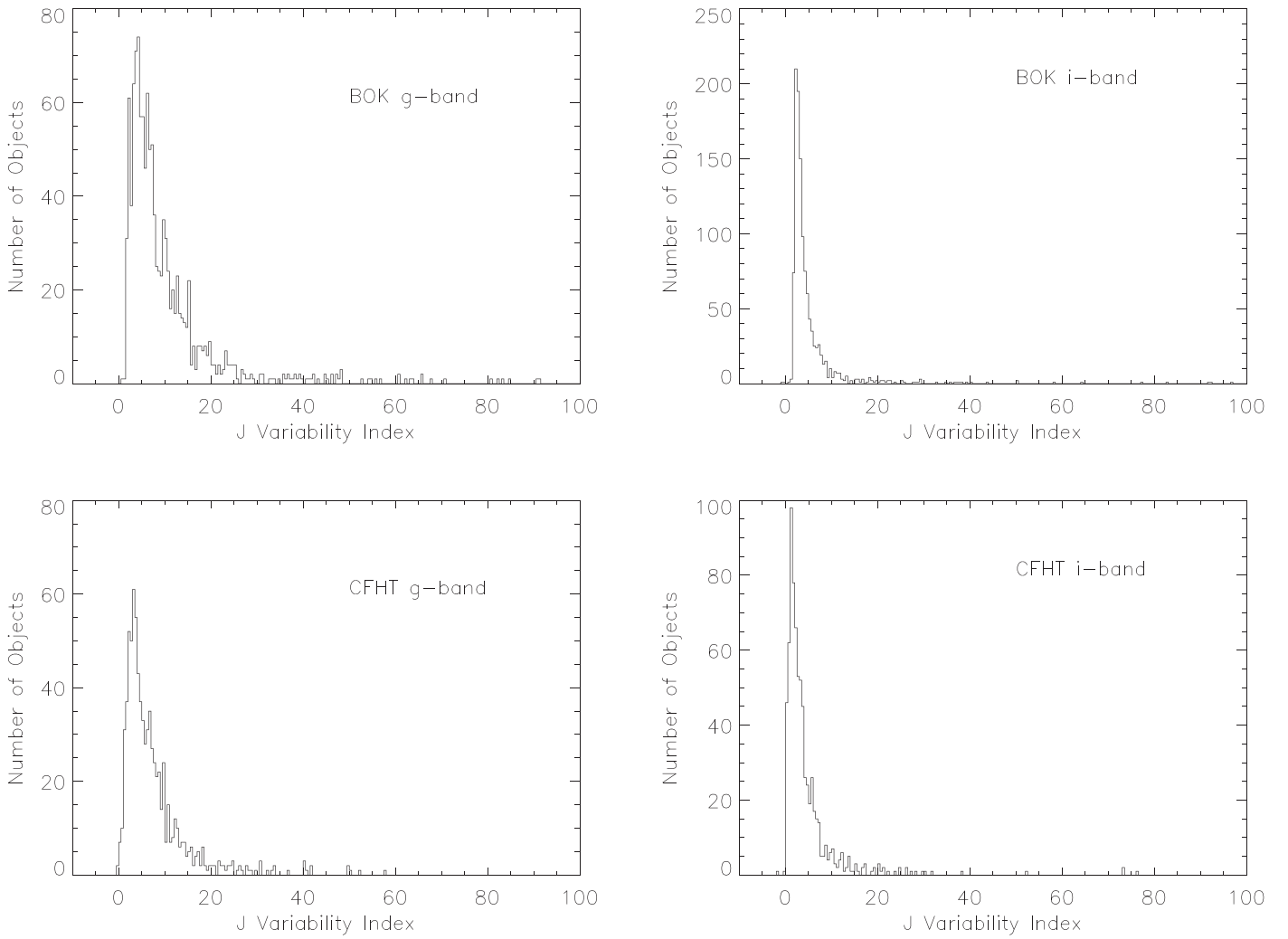


Figure 3. Distribution of the J variability indices for the SDSS-RM AGNs. Upper plots are for the J variability indices calculated from the Bok data sets. Lower plots are for the J indices calculated from the CFHT data sets. The left plots are for *g*-band data and the right plots are for *i*-band data.

Table 4
SDSS-RM Objects with the Welch–Stetson Variability Index in the SDSS *g* and *i* Bands

RM ID	α (J2000.0)	δ (J2000.0)	z (kpc)	<i>g</i> mag	<i>i</i> mag	Bok <i>g</i> Var Idx	Bok <i>i</i> Var Idx	CFHT <i>g</i> Var Idx	CFHT <i>i</i> Var Idx
0	213.697906	53.065586	1.4819	22.388	21.641	7.946	4.394	9.484	2.111
1	213.654312	53.073048	1.4628	21.250	20.837	9.161	1.527	3.309	1.370
2	213.774719	53.060932	1.2880	21.060	20.669	5.440	2.411	4.163	...
3	213.673996	53.149841	2.2371	22.271	21.730	5.686	3.034	2.882	1.220
4	213.756454	53.016392	1.7572	21.926	21.629	6.438	1.450	5.666	1.692
5	213.814209	53.116009	0.7585	20.638	20.262	3.426	2.671

(This table is available in its entirety in machine-readable form.)

foreground star would dominate and inflate the sky background. In such problematic subfields, fewer images could be included in the construction of a robust reference image.

Each CCD has a small FoV and typically contained 2–8 AGNs. We selected ~ 100 reference stars in each subfield along with the AGNs. We used the standard stars’ light curves to rescale the uncertainties and correct for any offsets between the years (e.g., due to the filter change—see Section 2.1).

Once the image quality had been assessed and all the targets identified in the fields, we began the ISIS difference imaging

processing by doing an interpolation of the images, reference image creation, image subtraction of the convolved images to the reference image, and finally PSF photometry of the residual images.

3.2. Bok Processing

The data set from the Bok 90Prime telescope spanned the observational season of the SDSS-RM field from 2014 to 2017. The field was observed in mostly bright time, which allowed

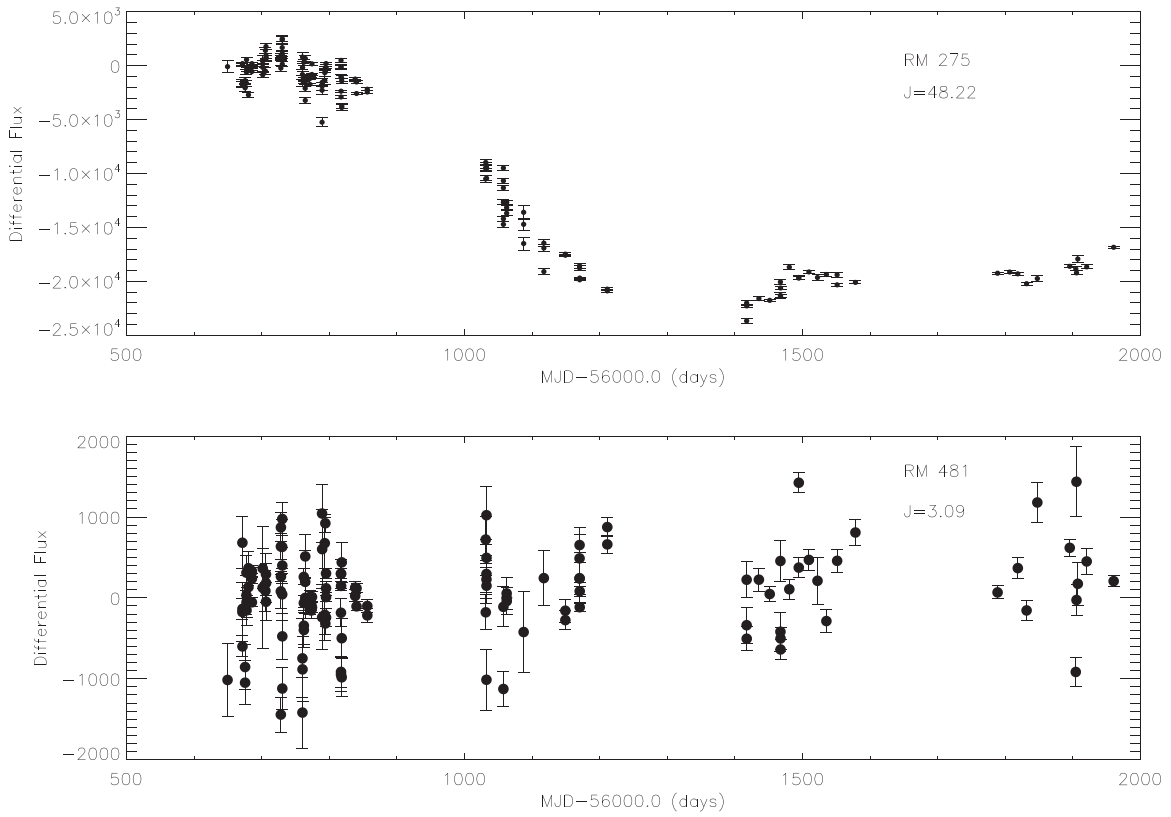


Figure 4. (Upper) Light curve of RM 275, which has large, long-term variation. RM 275 has a calculated variability index of $J = 48.22$. RM 275 has a g -band magnitude of 20.73. The photometric error bars are negligible with respect to the range in flux presented here. In the ISIS convention, a negative differential flux means the source is mostly brighter than on the reference image. (Lower) Photometric light curve of RM 481, which appears to have relatively small variation between 2014 and 2017. This AGN has a g -band magnitude of 20.74 and a variability index of $J = 3.09$.

coverage of the variability during the times when the field was not observed by SDSS or CFHT. The bulk of the data were primarily taken during 2014, and it is this data set that serves as the baseline for the difference imaging processing of the subsequent years of Bok data.

The Bok data from 2014 were processed with ISIS mostly using the same procedures as for the CFHT 2014 data, but with a few changes. One extra step in the preparatory work done to the Bok images was to add back in the sky background value, as this information was removed from the reduced images from the Bok pipeline. Without this sky background information, ISIS had difficulty producing a useful reference image as well as convolving the rest of the images because ISIS assumes the sky is included. This particular step was done only for the 2014 data set. In the 2015–2017 data reduction, the sky background was retained. Next, the image with the best FWHM and lowest sky background was identified, and the other images were interpolated to its reference frame. This reference image (which was based on primarily 2014 images) was the basis for the later, incorporated Bok data sets. Since the Bok fields had a larger FoV, more reference stars were available and processed per field. The standard stars were used to rescale the uncertainties in the flux measurements of the SDSS-RM AGNs (see Grier et al. 2017).

In addition to the original 849 RM targets from Shen et al. (2015a), 365 objects were also identified as possible AGN in the Bok fields. These extra 365 targets currently lack spectroscopic data and only have Bok time-series photometry spanning the 4 yr. These AGNs are in the CFHT data, but at the time of the ISIS processing, the information for these extra objects were not available, and thus they were not processed.

4. RM Target Light Curves

For the photometric light curves, we include with this paper the ISIS output from its *phot* module of the ISIS software. The output photometry files are provided as online data and are archived as a multi-extension FITS file. The columns in the output photometry files are as follows:

1. *Column 1.* Midpoint of the observation in MJD (days).
2. *Column 2 and 4.* Differential fluxes.
3. *Column 3 and 5.* Respective uncertainties in the differential flux measurement of Column 2 and 4.
4. *Column 6 and 7.* Sky background measurements.
5. *Column 8.* The local average sky value over N_{sky} pixels.
6. *Column 9.* The local median sky value over N_{sky} pixels.
7. *Column 10.* N_{sky} pixels used in Column 8 and 9.
8. *Column 11.* The aperture flux measured over N pixels.
9. *Column 12.* The number of pixels, N .

The fluxes are in units of counts but are all on the flux scale of their reference image. Two differential flux values are calculated, which are based on two different PSF weighting schemes for extracting the fluxes. Any significant difference between these fluxes is an indication of subtraction problems usually due to a nearby bright source, clouds, or other systematic problems. ISIS itself assumes clean subtractions, in which case the “sky” on a subtracted image is consistent with zero. However, clouds can produce a local, variable “sky” in the subtracted images, and we use a modified code that attempts to correct for a local sky. For our analysis we used the flux and uncertainty values of Columns 2 and 3. The actual photometric noise may be larger, by up to a factor of 2,

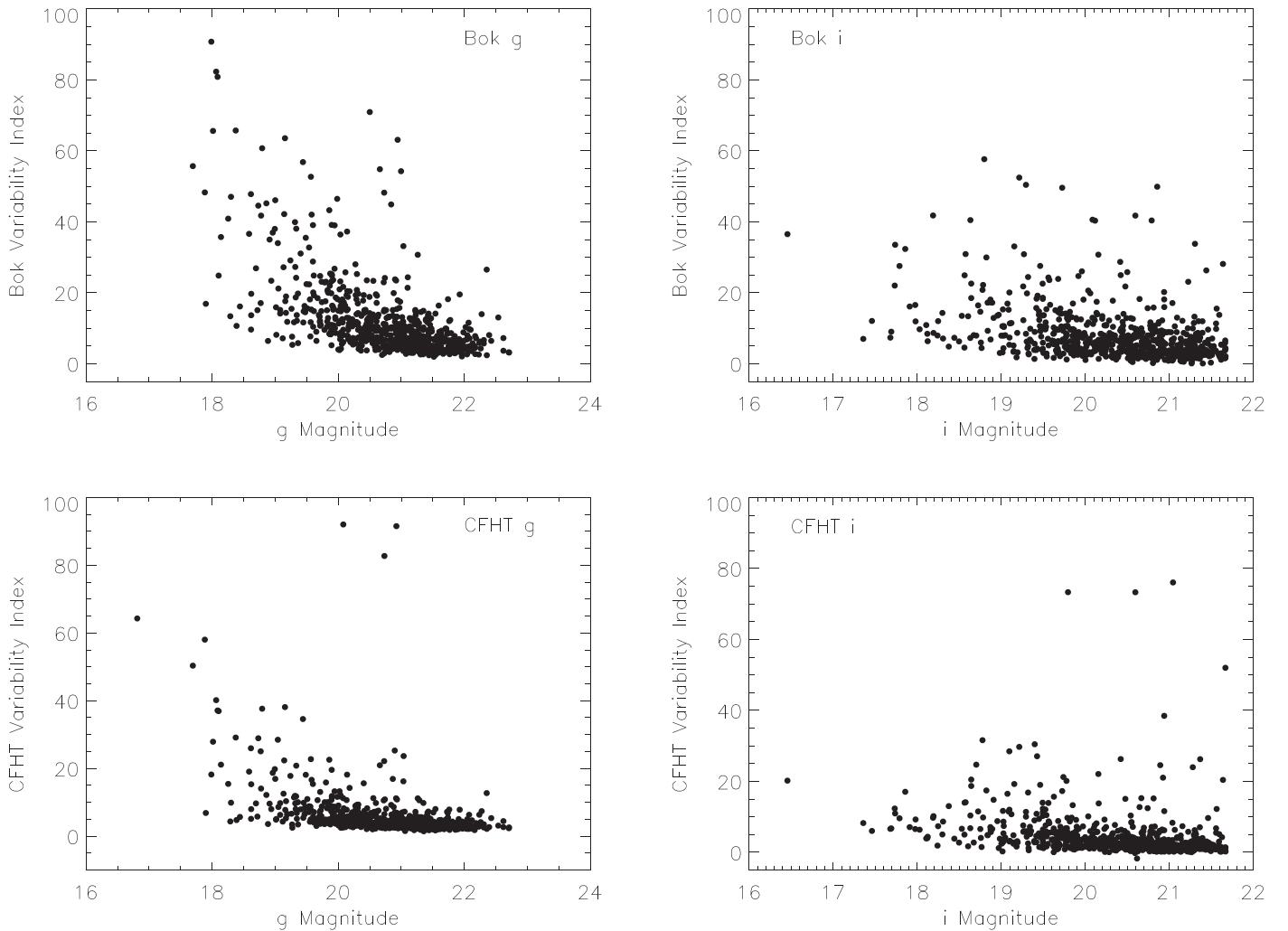


Figure 5. (Upper) Bok g - and i -band variability indices as a function of magnitude for the SDSS-RM AGNs. (Lower) CFHT g - and i -band J indices as a function of magnitude.

compared to what is reported in Columns 3 and 5. The crude aperture flux value in Column 11 can be used as a sanity check against the flux values determined in Columns 2 and 4. In the ISIS convention, a negative flux on the subtracted image means the source is brighter than on the reference image. To convert the differential flux to a magnitude, the flux of the object from the reference image must be subtracted to the *differential flux*. These differential flux values are all with respect to the reference images used in the processing. We intend to provide the reference flux values of the AGNs in a later paper after incorporating additional data sets that are being collected now.

Since the FoV of both the CFHT and Bok data sets are relatively large, we can see variable cloud cover in the frames. The differential flux scalings are affected by this cloud cover and by the halos of bright, foreground stars. In both cases, the sky background values can be nonzero and can be checked with the values in Column 6 and 7 of the ISIS output files. A number of targets found close to the edge of a CCD may have fewer epochs due to the object occasionally falling off the edge of the image. Due to the dithering, the edges of the reference image are some 20 pixels inward from the nominal chip edge. The software would discard flux measurements of targets from these edge regions due to problems such as poor PSF profiles.

In some cases, these edge targets have fluxes measured from an adjacent subfield, so the light curves can still be constructed.

5. Measuring AGN Variations

The photometric data set we present here provides an excellent opportunity to apply a variability index, which can be used to select interesting targets for further study. We characterized the variability with the Welch–Stetson J index, which was originally developed for identifying pulsating variable stars (Welch & Stetson 1993; Stetson 1996). We calculated the J index using both the Bok and CFHT data sets; however, the Bok data set has the advantage of having more epochs, which yielded a more robust variability index. The description of the Welch–Stetson J-index construction is provided in the [Appendix](#). For a more thorough description of this analysis tool, we direct the reader to Stetson (1996).

5.1. Application of the Variability Index

We calculated the variability index for all 849 SDSS-RM objects using both the Bok and CFHT g and i data. We also calculated the Welch–Stetson J index for the additional 365 AGN (Shen et al. 2019) with the Bok data. These additional

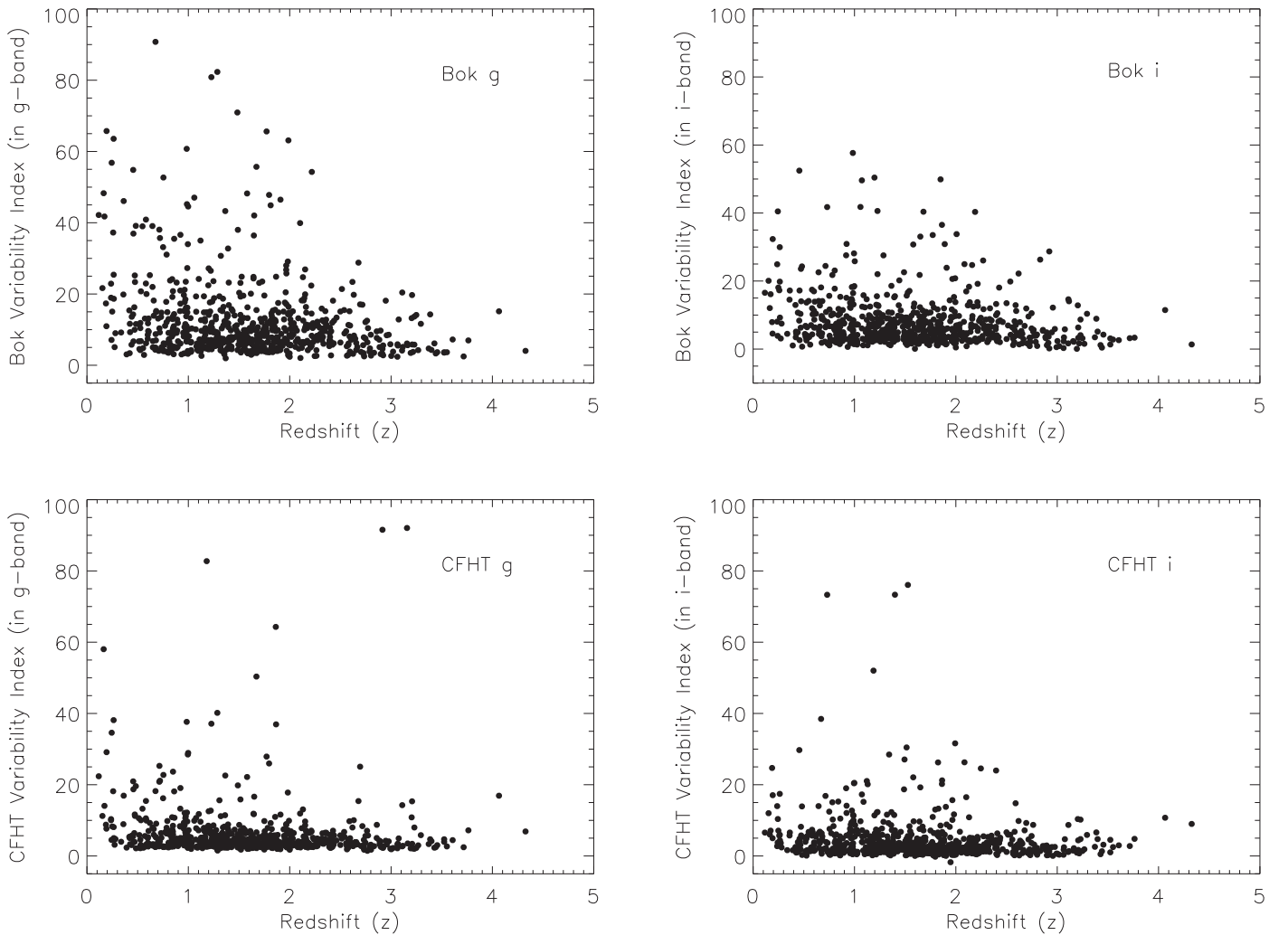


Figure 6. Distribution of J indices, constructed from g - and i -band data, as a function of redshift, z . (Upper) J indices were calculated from Bok data sets while (lower) plots have J indices based from the CFHT data sets.

AGN were not processed in the CFHT data sets, since at the time of the differential flux processing, the positions of those objects were not available. Subsequent ISIS processing of the CFHT data set is planned to include these additional AGNs. The Bok data set has more epochs and a longer time baseline. Thus, the Bok variability index should be more accurate and better reflect the variable nature of the AGN. We find that the J-index values calculated from the CFHT data set are consistent with the values based on the Bok data sets. We provide the J variability index for each SDSS-RM AGN in Table 4. In Figure 3, we present histograms of the J index with respect to the filter and telescope. Our calculation of the J index took into account of the case where an AGN was observed over different subfields due to the dithering of the field. Separate J indices were determined for the table, and we averaged those values.

Grier et al. (2017) examined 220 AGNs of the SDSS-RM sample for RM lags between the continuum and the $H\beta$ line. To select AGNs that were variable, they used a measurement of the rms scatter about the mean to quantify the variability. Their method differs from the formulation of the Welch–Stetson index; however, a visual inspection of the light curves indicates that both measurements track AGN variability well.

We note that there were several differences in the treatment of the light curves before these variability measurements were

made. For example, Grier et al. (2017) merged the light curves from the different data sets and corrected the flux uncertainties from the original ISIS fluxes. In our work, we adopted the differential flux values without any correction. Thus, a direct comparison between our J index and their rms variability measurement is not feasible.

Determining what level of variability measurement constitutes “significant” variability is somewhat subjective. Our visual inspection of the 220 AGN sample suggests that the J index is well correlated with the actual variability (both in the short and long-term). In Figure 4, the light curves of two AGNs with similar g magnitudes show how the J index can be used to pick out highly variable objects. RM 275 has a larger J-index value compared to RM 481, and their light curves exhibit their levels of variation reflecting their different variability indices. We provide here the J variability index as a guide for readers to select interesting objects for future projects. An example of a large variability index indicating activity in an AGN is RM 17, which is described as a hypervariable quasar by Dexter et al. (2019).

Figure 5 presents the variability index with respect to the g and i magnitudes of the SDSS-RM objects. We show in this figure the distribution of the indices from the Bok data sets and the CFHT data sets. At brighter magnitudes, larger variability

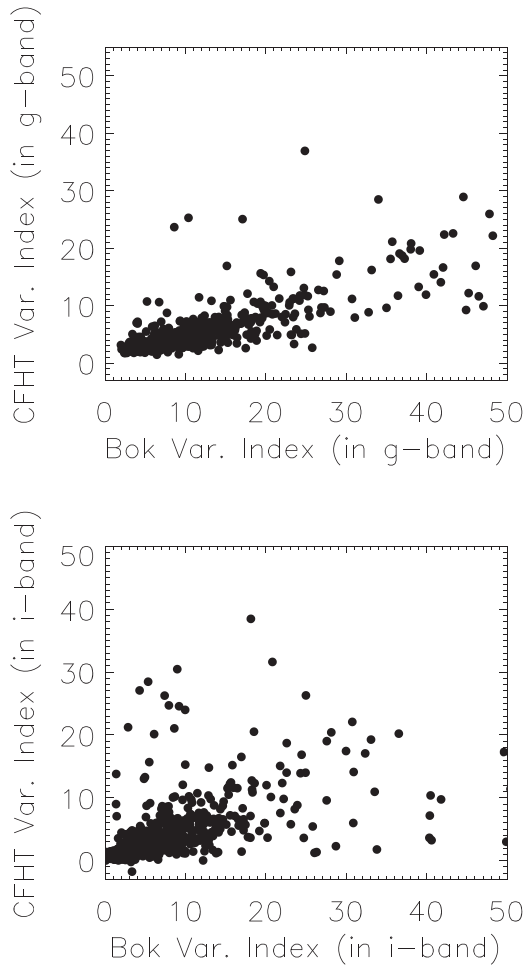


Figure 7. Comparison of the Welch–Stetson J index constructed from Bok and CFHT data. The upper panel is the comparison of J index based on the *g*-band data. The lower panel is for the J index based on the *i*-band data.

indices are seen, but at fainter magnitudes, we find fewer objects with such a level of variability. This result could be due to an observational bias in the sample, but in general, objects with large variations at brighter magnitudes are more readily identified in a sample.

To check this conclusion, we plot the J index against redshifts from Shen et al. (2015a). Figure 6 shows the distribution of the variability index with redshift. There remains a trend of larger variation in nearby AGNs, but this level of large variation is visible through the whole range of redshift. One of the goals of the SDSS-RM project is to study the AGN activity for a wide range of redshifts. The presence of different levels of variation across all redshifts in the SDSS-RM sample confirms that reverberation mapping should be feasible over this range with no preselection on quasar variable properties.

To understand the J index calculated from data taken at two different telescopes, we plot the indices from the *g*- and *i*-band data in Figure 7. There is no one-to-one correlation between the J indices calculated from the Bok and CFHT data. The reason for the typically larger J index for Bok data could be due to the differing S/Ns of the individual images from each telescope. The uncertainties of the flux measurements are folded into the J-index calculation (see the Appendix for more details), and the *g*-band uncertainties are smaller per Bok exposure. Thus, the Bok J-index values will appear to have a larger variation

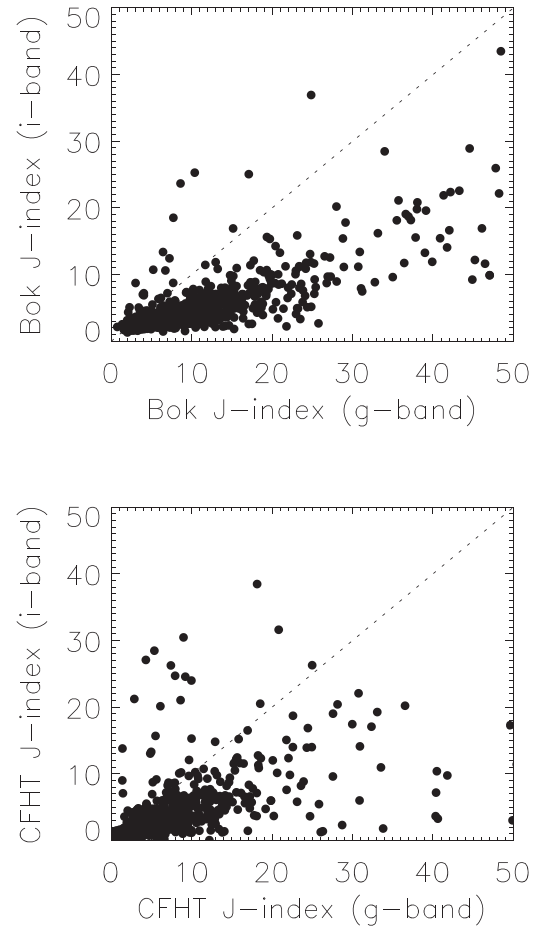


Figure 8. Comparison of the J indices constructed from *g*- and *i*-band data. A one-to-one line is provided to show that the quasars are more variable at shorter wavelengths. Upper panel: J index based on Bok data. Lower panel: J index based on CFHT data.

compared to the J index based on the CFHT data sets, for both *g* and *i* bandpasses. As mentioned above, the Bok data set has more epochs and a longer time baseline than the CFHT data set. Variability will be more likely to be detected in the Bok data than with the CFHT data.

Further, we compared separately the J index calculated based by telescope. In Figure 8, we compare the J index based on *g*- and *i*-band data, and again, we do not see a clear one-to-one correlation. In this case, the *g*-band J index shows a higher variability value than the *i*-band-based data. The variability in amplitudes are generally larger in shorter wavelengths (e.g., MacLeod et al. 2010). This is likely due to a combination of local accretion disk temperature changes being more evident with shorter wavelengths and effective disk areas being smaller with shorter wavelength, the latter leading to shorter-wavelength flux more closely tracking variations in the illuminating flux from the innermost regions of the accretion flow. In Figure 8, we added the one-to-one trend line to help guide the eye and to emphasize how it is clearly not one-to-one.

6. Summary

We present the photometric data sets for the SDSS-RM AGNs obtained at the CFHT and Bok telescopes over a span of 4 yr (2014–2017). We applied ISIS, a differential flux photometry technique, to the time-series data, and we calculated a variability

measure, the Welch–Stetson J index. The variability index can be used to select interesting AGNs for further study. We find that many of the variable AGNs in this sample have long-term variability (i.e., the variation occurs over years rather than days). We were able to identify objects with low levels of variability that appear to be significant and above the noise level. Almost all the objects in this study appear to have some level of variation in their continuum flux over the course of the observations.

There are many projects currently underway using these photometric data. The SDSS-RM team has been merging the Bok and CFHT data sets with the SDSS–BOSS spectra to analyze the various lags seen in the AGNs (see Grier et al. 2017, 2019). The photometry is also being used to measure interband continuum lags in quasars to learn about the accretion disk size (Homayouni et al. 2019). Over 200 AGNs from the original SDSS-RM sample have merged Bok and CFHT light curves that have been published by Grier et al. (2017), and more are expected to be merged and analyzed for future projects (e.g., Grier et al. 2019; Homayouni et al. 2019, 2020).

Based in part on observations obtained with MegaPrime/MegaCam, a joint project of CFHT and CEA/DAPNIA, at the CFHT, which is operated by the National Research Council (NRC) of Canada, the Institut National des Sciences de l’Univers of the Centre National de la Recherche Scientifique of France, and the University of Hawaii.

The authors wish to recognize and acknowledge the very significant cultural role and reverence that the summit of Maunakea has always had within the indigenous Hawaiian community. We are most fortunate to have the opportunity to conduct observations from this mountain.

We thank the CFHT staff who supported our program, including Nadine Manset, Todd Burdullis, Simon Prunet, and Andreea Petric.

We thank the anonymous referee for the helpful comments to this paper.

P.H. acknowledges the support of the Natural Sciences and Engineering Research Council of Canada (NSERC), funding reference number 2017-05983. C.J.G., W.N.B., and D.P.S. acknowledge support from NSF grant AST-1517113. Y.S. acknowledges support from an Alfred P. Sloan Research Fellowship and NSF grant AST-1715579. L.C.H. acknowledges the National Key R&D Program of China (2016YFA0400702) and the National Science Foundation of China (11721303, 11991052). J.V.H.S. and K.H. acknowledge support from a STFC grant ST/R000824/1. C.S.K. is supported by NSF grants AST-1814440 and AST-1908570.

Appendix

The Welch–Stetson J Variability Index

The Welch–Stetson J index (or simply the J index) has many features that best incorporate the SDSS-RM photometric data sets to produce a robust quantification of the AGN variation. The J index takes advantage of the observing cadence, specifically if there were paired epochs close in time. For the Bok data, two observations were taken of each subfield, depending on the sky conditions. We can also calculate the J index for unpaired, single epochs. This feature allows us to use all of the observations rather than tossing out unpaired epochs. To define a “pair” of observations from a night’s data set, we selected a minimum time interval between observations of 0.005 days (7 minutes). Any two observations taken within this

interval were considered to be a “pair”; any observation taken outside of this interval was considered to be part of another (subsequent) observation or pair. If an observation does not have a closely timed observation, it was considered to be a “single” observation of that subfield. In our data sets, we assume the second of a pair of observations was collected within 7 minutes after the collection of the first observation. This time interval can be adjusted to define “paired” observations for a specific data set.

Another strength of the J index is that it uses information from two different bandpasses. For variable stars, the variation is often correlated with color due to the nature of the stellar pulsation. However, for AGNs, the observed variability in the light curve does not necessarily correlate in g and i at the same moment in time as time delays between the g - and i -band continuum fluxes have been observed (e.g., Shappee et al. 2014; Fausnaugh et al. 2016, 2018; Homayouni et al. 2019; Cackett et al. 2020). Thus, we chose not to combine the g and i data sets in the construction of the J index.

The J index is composed of the relative error (δ), normalized residuals of a pair of observations (P_k), and a weighting factor (w_k). Stetson (1996) defines the relative error as the residual from a mean magnitude, weighted by the measurement’s uncertainty and the number of observations, n , as

$$\delta_i = \frac{f_i - \bar{f}}{\sigma_{f,i}} \sqrt{\frac{n}{n-1}}. \quad (\text{A1})$$

In the case of our data set, we do not use magnitudes, but differential flux values from ISIS, thus in Equation (A1), instead of using Stetson (1996)’s “ v magnitude,” we are using “ f ” for the differential flux.

As described in Stetson (1987, 1996), we follow the prescription to obtain a robust weighted mean flux value through iteration. When the initial weighted mean flux value has been determined from Equation (A1), we recalculate the weight by its residual error. This weight of an observation is defined as

$$w_i = \left[1 + \left(\frac{|\delta_i|}{2} \right)^2 \right]^{-1}. \quad (\text{A2})$$

The following equation is used for the calculation for the weighted mean flux from Welch & Stetson (1993, their Equation (1) and (2), computed in terms of flux):

$$\bar{f} = \frac{\sum_{i=1}^n \frac{f_i}{\sigma_{f,i}^2}}{\sum_{i=1}^n \frac{1}{\sigma_{f,i}^2}}. \quad (\text{A3})$$

For our weighted mean flux, \bar{f} , we iterated five times to reach a stable value and to minimize the effects of any large outliers in the light curve data. We found that increasing the number of iterations did not change the value of the mean flux significantly. A quick visual inspection revealed that some of the light curves did show a real, large outlier from the photometry. To help aid in the robustness of our variability index, we removed any large, obvious outliers that were 3σ from our weighted mean flux. In some cases, a single outlier did influence the calculation of the variability index, and with 3σ clipping, we have a more robust index value.

For a pair of closely timed data points, the product of the residual errors can be constructed from the i th and j th observations. This product is identified as the normalized

residuals of the k th pair

$$P_k = \delta_i \delta_j. \quad (\text{A4})$$

The normalized residual for a single observation can be simplified to

$$P_k = \delta_i^2 - 1. \quad (\text{A5})$$









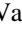

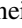
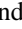









The J index is calculated from Equation (A6). The sgn function simply returns the sign of the expression, whether it is positive or negative. The subscript k refers to the paired observation. We use the weighting factor determined from Equation (A2) here for the J variability index. In this weighting factor, we use the residual error of the pair or single observation and does not require iteration used with the weighted mean flux.

$$J = \frac{\sum_{k=1}^n w_k \text{sgn}(P_k) \sqrt{|P_k|}}{\sum_{k=1}^n w_k}. \quad (\text{A6})$$

The advantage of using paired observations compared to single observations is that the P_k quantity will be positive in most cases. The individual residual errors will be positive for fluxes far above the weighted mean or negative for fluxes far below. A quasar with strong variability can have P_k values ranging from small to large values, but the sum will produce a large J-index value.

In a few cases, Equation (A6) yielded a negative value. Stetson (1996) describes how cosmetic defects or problems with the data processing can produce this negative value. We identified four AGNs with a negative J values in the Bok data set, and upon inspection of the reference frame, all of these objects are found near the edge of a CCD where the PSF photometry can fail.

ORCID iDs

K. Kinemuchi  <https://orcid.org/0000-0001-7908-7724>
 Patrick B. Hall  <https://orcid.org/0000-0002-1763-5825>
 Ian McGreer  <https://orcid.org/0000-0002-3461-5228>
 C. S. Kochanek  <https://orcid.org/0000-0001-6017-2961>
 Catherine J. Grier  <https://orcid.org/0000-0001-9920-6057>
 Jonathan Trump  <https://orcid.org/0000-0002-1410-0470>
 Yue Shen  <https://orcid.org/0000-0003-1659-7035>
 W. N. Brandt  <https://orcid.org/0000-0002-0167-2453>
 W. M. Wood-Vasey  <https://orcid.org/0000-0001-7113-1233>
 Xiaohui Fan  <https://orcid.org/0000-0003-3310-0131>
 Bradley M. Peterson  <https://orcid.org/0000-0001-6481-5397>
 Donald P. Schneider  <https://orcid.org/0000-0001-7240-7449>
 Juan V. Hernández Santisteban  <https://orcid.org/0000-0002-6733-5556>
 Keith Horne  <https://orcid.org/0000-0003-1728-0304>
 Siyao Jia  <https://orcid.org/0000-0001-5341-0765>
 Kara A. Ponder  <https://orcid.org/0000-0002-8207-3304>
 Jesse Rogerson  <https://orcid.org/0000-0002-7078-1776>
 Tianmen Zhang  <https://orcid.org/0000-0002-8531-5161>
 Hu Zou  <https://orcid.org/0000-0002-6684-3997>
 Linhua Jiang  <https://orcid.org/0000-0003-4176-6486>
 Luis C. Ho  <https://orcid.org/0000-0001-6947-5846>
 Nathalie Palanque-Delabrouille  <https://orcid.org/0000-0003-3188-784X>

References

- Alard, C. 2000, *A&AS*, **144**, 363
 Alard, C., & Lupton, R. 1999, ISIS: A Method for Optimal Image Subtraction, Astrophysics Source Code Library, ascl:9909.003
 Alard, C., & Lupton, R. H. 1998, *ApJ*, **503**, 325
 Aune, S., Boulade, O., Charlot, X., et al. 2003, *Proc. SPIE*, **4841**, 513
 Barlow, T. A. 1993, PhD thesis, Univ. California San Diego
 Bertin, E. 2006, in ASP Conf. Ser. 351, Astronomical Data Analysis Software and Systems XV, ed. C. Gabriel et al. (San Francisco, CA: ASP), **112**
 Bertin, E., & Arnouts, S. 1996, *A&AS*, **117**, 393
 Blandford, R. D., & McKee, C. F. 1982, *ApJ*, **255**, 419
 Blanton, M. R., Bershad, M. A., Abolfathi, B., et al. 2017, *AJ*, **154**, 28
 Cackett, E. M., Gelbord, J., Li, Y.-R., et al. 2020, *ApJ*, **896**, 1
 Clavel, J., Reichert, G. A., Alloin, D., et al. 1991, *ApJ*, **366**, 64
 Clavel, J., Wamsteker, W., & Glass, I. S. 1989, *ApJ*, **337**, 236
 Cohen, R. D., Rudy, R. J., Puetter, R. C., et al. 1986, *ApJ*, **311**, 135
 Czerny, B., Schwarzenberg-Czerny, A., & Loska, Z. 1999, *MNRAS*, **303**, 148
 Denney, K. D., De Rosa, G., Croxall, K., et al. 2014, *ApJ*, **796**, 134
 Denney, K. D., Horne, K., Brandt, W. N., et al. 2016a, *ApJ*, **833**, 33
 Denney, K. D., Horne, K., Shen, Y., et al. 2016b, *ApJS*, **224**, 14
 Dexter, J., Xin, S., Shen, Y., et al. 2019, *ApJ*, **885**, 44
 Fausnaugh, M. M., Denney, K. D., Barth, A. J., et al. 2016, *ApJ*, **821**, 56
 Fausnaugh, M. M., Starkey, D. A., Horne, K., et al. 2018, *ApJ*, **854**, 107
 Filiz, A. N., Brandt, W. N., Hall, P. B., et al. 2013, *ApJ*, **777**, 168
 Grier, C. J., Hall, P. B., Brandt, W. N., et al. 2015, *ApJ*, **806**, 111
 Grier, C. J., Shen, Y., Horne, K., et al. 2019, *ApJ*, **887**, 38
 Grier, C. J., Trump, J. R., Shen, Y., et al. 2017, *ApJ*, **851**, 21
 Hemler, Z. S., Grier, C. J., Brandt, W. N., et al. 2019, *ApJ*, **872**, 21
 Homayouni, Y., Trump, J. R., Grier, C. J., et al. 2019, *ApJ*, **880**, 126
 Homayouni, Y., Trump, J. R., Grier, C. J., et al. 2020, *ApJ*, in press (arXiv:2005.03663)
 Kaspi, S., Smith, P. S., Netzer, H., et al. 2000, *ApJ*, **533**, 631
 Kelly, B. C., Sobolewska, M., & Siemiginowska, A. 2011, *ApJ*, **730**, 52
 King, A. L., Martini, P., Davis, T. M., et al. 2015, *MNRAS*, **453**, 1701
 Kollmeier, J. A., Zasowski, G., Rix, H.-W., et al. 2017, arXiv:1711.03234
 Kozłowski, S., Kochanek, C. S., Udalski, A., et al. 2010, *ApJ*, **708**, 927
 Krolik, J. H., Horne, K., Kallman, T. R., et al. 1991, *ApJ*, **371**, 541
 LaMassa, S. M., Cales, S., Moran, E. C., et al. 2015, *ApJ*, **800**, 144
 Li, J., Shen, Y., Horne, K., et al. 2017, *ApJ*, **846**, 79
 Lindegren, L., Lammers, U., Bastian, U., et al. 2016, *A&A*, **595**, A4
 Lundgren, B. F., Wilhite, B. C., Brunner, R. J., et al. 2007, *ApJ*, **656**, 73
 MacLeod, C. L., Ivezić, Ž., Kochanek, C. S., et al. 2010, *ApJ*, **721**, 1014
 MacLeod, C. L., Ross, N. P., Lawrence, A., et al. 2016, *MNRAS*, **457**, 389
 Matsuoka, Y., Strauss, M. A., Shen, Y., et al. 2015, *ApJ*, **811**, 91
 Peterson, B. M. 1993, *PASP*, **105**, 247
 Peterson, B. M., Ferrarese, L., Gilbert, K. M., et al. 2004, *ApJ*, **613**, 682
 Semboloni, E., Mellier, Y., van Waerbeke, L., et al. 2006, *A&A*, **452**, 51
 Shappee, B. J., Prieto, J. L., Grupe, D., et al. 2014, *ApJ*, **788**, 48
 Shen, Y., Brandt, W. N., Dawson, K. S., et al. 2015a, *ApJS*, **216**, 4
 Shen, Y., Brandt, W. N., Richards, G. T., et al. 2016a, *ApJ*, **831**, 7
 Shen, Y., Greene, J. E., Ho, L. C., et al. 2015b, *ApJ*, **805**, 96
 Shen, Y., Hall, P. B., Horne, K., et al. 2019, *ApJS*, **241**, 34
 Shen, Y., Horne, K., Grier, C. J., et al. 2016b, *ApJ*, **818**, 30
 Smee, S. A., Gunn, J. E., Uomoto, A., et al. 2013, *AJ*, **146**, 32
 Smith, L. J., & Penston, M. V. 1988, *MNRAS*, **235**, 551
 Stetson, P. B. 1987, *PASP*, **99**, 191
 Stetson, P. B. 1996, *PASP*, **108**, 851
 Sun, M., Grier, C. J., & Peterson, B. M. 2018, PyCCF: Python Cross Correlation Function for reverberation mapping studies, Astrophysics Source Code Library, ascl:1805.032
 Sun, M., Trump, J. R., Shen, Y., et al. 2015, *ApJ*, **811**, 42
 Tohline, J. E., & Osterbrock, D. E. 1976, *ApJL*, **210**, L117
 Turnshek, D. A., Foltz, C. B., Grillmair, C. J., et al. 1988, *ApJ*, **325**, 651
 Ulrich, M.-H., Maraschi, L., & Urry, C. M. 1997, *ARA&A*, **35**, 445
 Vanden Berk, D. E., Wilhite, B. C., Kron, R. G., et al. 2004, *ApJ*, **601**, 692
 Wang, S., Shen, Y., Jiang, L., et al. 2019, *ApJ*, **882**, 4
 Welch, D. L., & Stetson, P. B. 1993, *AJ*, **105**, 1813
 Williams, G. G., Olszewski, E., Lesser, M. P., & Burge, J. H. 2004, *Proc. SPIE*, **5492**, 787
 Yue, M., Jiang, L., Shen, Y., et al. 2018, *ApJ*, **863**, 21